# Assimilation of Surface-Based Boundary Layer Profiler Observations during a Cool-Season Weather Event Using an Observing System Simulation Experiment. Part I: Analysis Impact

JASON A. OTKIN AND DANIEL C. HARTUNG

*Cooperative Institute for Meteorological Satellite Studies, University of Wisconsin—Madison, Madison, Wisconsin*

DAVID D. TURNER

*NOAA/National Severe Storms Laboratory, Norman, Oklahoma, and Department of Atmospheric and Oceanic Sciences, University of Wisconsin—Madison, Madison, Wisconsin*

RALPH A. PETERSEN AND WAYNE F. FELTZ

*Cooperative Institute for Meteorological Satellite Studies, University of Wisconsin—Madison, Madison, Wisconsin*

ERIK JANZON

*Department of Atmospheric and Oceanic Sciences, University of Wisconsin—Madison, Madison, Wisconsin*

(Manuscript received 10 September 2010, in final form 10 February 2011)

ABSTRACT

In this study, an Observing System Simulation Experiment was used to examine how the assimilation of temperature, water vapor, and wind profiles from a potential array of ground-based remote sensing boundary layer profiling instruments impacts the accuracy of atmospheric analyses when using an ensemble Kalman filter data assimilation system. Remote sensing systems evaluated during this study include the Doppler wind lidar (DWL), Raman lidar (RAM), microwave radiometer (MWR), and the Atmospheric Emitted Radiance Interferometer (AERI). The case study tracked the evolution of several extratropical weather systems that occurred across the contiguous United States during 7–8 January 2008. Overall, the results demonstrate that using networks of high-quality temperature, wind, and moisture profile observations of the lower troposphere has the potential to improve the accuracy of wintertime atmospheric analyses over land. The impact of each profiling system was greatest in the lower and middle troposphere on the variables observed or retrieved by that instrument; however, some minor improvements also occurred in the unobserved variables and in the upper troposphere, particularly when RAM observations were assimilated. The best analysis overall was achieved when DWL wind profiles and temperature and moisture observations from the RAM, AERI, or MWR were assimilated simultaneously, which illustrates that both mass and momentum observations are necessary to improve the analysis accuracy.

## 1. Introduction

Accurate observations of the atmosphere provide the framework to understand physical processes at various scales and are essential for weather forecasting applications and long-term trend analysis. Environmental observations play a significant role in our lives, as weather and climate impact agriculture, transportation, personal safety, dispersion modeling, and homeland security. As such, a large number of private companies, universities, and state and federal government agencies have developed and deployed meteorological instruments across the United States in order to collect data to support these and other applications.

*Corresponding author address:* Jason A. Otkin, University of Wisconsin—Madison, 1225 W. Dayton St., Madison, WI 53706.
E-mail: jason.otkin@ssec.wisc.edu

DOI: 10.1175/2011MWR3622.1

The National Research Council (NRC) recently issued a report on the existing array of meteorological observing networks distributed across the United States (National Research Council 2009). In this report, the NRC found that the current surface-based meteorological observation capabilities are energetic, but also chaotic and driven mainly by local needs without adequate coordination between networks. To remedy this situation, the report called for a more comprehensive and adaptive national strategy for ground-based observations, with an emphasis on the planetary boundary layer (PBL) where existing observation capabilities were found to be particularly inadequate. The PBL is very difficult to accurately characterize from space, and the current ground-based networks are too sparse and unevenly distributed to adequately describe the wind, temperature, and moisture structure of the boundary layer at high temporal and spatial resolution. Thus, the NRC suggested that a new coordinated network of ground-based profiling instruments should be deployed across the United States to address these observational deficiencies. In particular, the NRC recommended the creation of a network consisting of approximately 400 stations with instruments capable of profiling the humidity, wind, and temperature in and above the PBL over the complete diurnal cycle. The NRC considered this new network to be of the highest priority because these observations are essential to improving many applications such as the performance of high-resolution numerical weather prediction (NWP) models.

The University of Wisconsin—Madison has extensive experience with both active and passive ground-based thermodynamic profiling instruments (e.g., Feltz et al. 1998, 2003; Turner and Goldsmith 1999; Turner et al. 2000, 2002). To perform an analysis of different instruments that could potentially compose this network, an ensemble Kalman filter (EnKF; Evensen 1994) data assimilation system was used to conduct an Observing System Simulation Experiment (OSSE) for a cool-season weather event. Each profiling technique evaluated during the OSSE is sensitive to different components of the atmosphere with varying accuracy and resolution, and is characterized by different initial (e.g., purchase and installation) and long-term (e.g., maintenance and personnel) expenses. OSSEs have been used for decades to evaluate the merit of different observing strategies in a controlled and cost-effective manner (e.g., Arnold and Dey 1986; Kuo et al. 1987; Kuo and Guo 1989; Benjamin et al. 1991; Moninger et al. 2010), however, few studies have focused on the impact of locally concentrated remotely sensed profiler observations of the PBL over land. An EnKF assimilation system was chosen for this study because unlike variational methods it provides a time-varying estimate of the background error covariances used during the assimilation step and is also able to account for nonlinear processes in both the assimilation model and the forward observation operator. Flow-dependent error covariances are most useful when assimilating observations within regions that depart substantially from a climatological or static background field or are characterized by sharp gradients.

Several considerations were made when determining the parameters of this OSSE. First, because of timing restrictions by the funding agency and by hardware limitations, the impact of the additional observational network was limited to a single case study. Second, to reduce the potential installation and operation costs relative to establishing a set of new instrument sites, it was decided to locate the ground-based remote sensors at each of the Weather Surveillance Radar-1988 Doppler (WSR-88D) sites since they are relatively evenly distributed across the contiguous United States and already have the necessary infrastructure and manpower to operate additional instruments. The resultant 140 ground-based boundary layer profiling sites is less than the 400 recommended by the NRC; however, this analysis provides a reasonable first attempt to evaluate the impact of the additional profiler observations. Last, since the instruments deployed in the potential network must be run operationally, the analysis primarily considers commercially available systems proven to operate routinely over long time periods with little manual intervention. Profile observations were created to emulate the Doppler wind lidar (DWL), microwave radiometer (MWR), and Atmospheric Emitted Radiance Interferometer (AERI) sensors. Observations were also created to emulate the state-of-the-art Raman lidar (RAM) system run operationally at the Department of Energy's Atmospheric Radiation Measurement (ARM) site in north-central Oklahoma (Goldsmith et al. 1998; Turner et al. 2000, 2002); however, this sensor is currently not commercially available and requires greater manual intervention than the other sensors.

The paper is organized as follows. Section 2 contains a description of the forecast model, data assimilation system, and simulated observations. An overview of the case study is provided in section 3, results are shown in section 4, and conclusions are presented in section 5.

## 2. Experimental design

### a. Forecast model

Version 3.0.1.1 of the Weather Research and Forecasting (WRF) model was used for this study. WRF is a sophisticated NWP model that solves the compressible nonhydrostatic Euler equations cast in flux form on a mass-based terrain-following vertical coordinate system. Prognostic variables include the horizontal and vertical

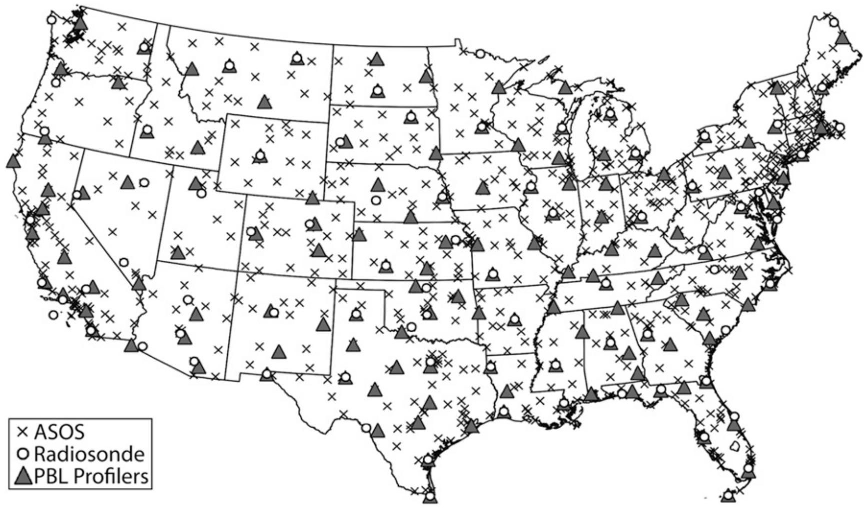


FIG. 1. Geographical region covered by the truth simulation and assimilation experiments. The ASOS (crisscross), radiosonde (open circle), and boundary layer profiler (filled triangle) station locations are also indicated.

wind components, various microphysical and thermodynamic parameters, and the perturbation potential temperature, geopotential, and surface pressure of dry air. The reader is referred to Skamarock et al. (2005) for a complete description of the WRF modeling system.

### b. *Data assimilation system*

Assimilation experiments were conducted using the EnKF algorithm implemented in the Data Assimilation Research Testbed (DART) system developed at the National Center for Atmospheric Research (Anderson et al. 2009). The assimilation algorithm is based on the ensemble adjustment Kalman filter described by Anderson (2001), which processes a set of observations serially and is mathematically equivalent to the ensemble square root filter described by Whitaker and Hamill (2002). The DART system includes tools that automatically compute temporally and spatially varying covariance inflation values during the assimilation step (Anderson 2007, 2009). To reduce sampling error resulting from a small ensemble size, horizontal and vertical covariance localization (Mitchell et al. 2002; Hamill et al. 2001) is performed using a compactly supported fifth-order correlation function following Gaspari and Cohn (1999).

### c. *Simulated observations*

Simulated observations were generated for three conventional observing systems and four potential surface-based boundary layer profiler systems using data from the high-resolution "truth" simulation described in section 3. Conventional observations include those from the Automated Surface Observing System (ASOS), the Aircraft Communications Addressing and Reporting System (ACARS), and radiosondes. As mentioned in the introduction, profile observations were created to emulate DWL, RAM, MWR, and AERI sensors, with the profilers located at existing WSR-88D locations in order to leverage existing infrastructure and personnel resources. Figure 1 shows the geographical distribution of the observations. The methodology used to generate the simulated observations is discussed in the remainder of this section.

#### 1) CONVENTIONAL OBSERVATIONS

Simulated 10-m wind speed and direction along with 2-m temperature and relative humidity observations were computed at existing ASOS station locations whereas vertical profiles of temperature, relative humidity, and horizontal wind speed and direction were produced for each radiosonde station location. Standard reporting conventions were followed so that each radiosonde profile contains not only mandatory level data, but also significant level data corresponding to features such as temperature inversions and rapid changes in wind speed and direction. Simulated ACARS temperature and wind observations were produced at the same locations as the real pilot reports listed in the Meteorological Assimilation Data Ingest Files (MADIS) for the OSSE case study period. Realistic measurement errors drawn from an uncorrelated Gaussian error distribution and based on a given sensor's accuracy specification were added to each observation.

#### 2) DWL PROFILER OBSERVATIONS

A DWL transmits a series of short infrared laser pulses (typically at 1.5 $\mu$m) into the atmosphere and then measures the intensity and frequency of the backscattered radiation relative to the outgoing laser energy. Aerosol particles with diameters close to the DWL wavelength are the primary scatterers of the emitted radiation. Given the small size of these particles, they are sufficiently small to be advected by the wind and serve as tracers of wind velocity. Thus, the Doppler shift in the frequency of the backscattered radiation is used to compute the radial wind velocity as a function of height above the sensor. A typical accuracy of the radial velocity is ~0.15 m $s^{-1}$, which is achieved by adding the return signal from thousands of laser pulses collected over several seconds. DWLs transmit pulses at different angles relative to zenith (e.g., 5°–15° off zenith in the north, south, east, and west directions) and from these observations the horizontal components of the wind field are computed. Since there is little molecular scattering at 1.5 $\mu$m, the signal-to-noise ratio drops off precipitously above the boundary layer where there are relatively few aerosol particles, therefore, the DWL is only able to provide high temporal (~10 s) and vertical (~30 m) resolution wind data in the boundary layer. Additional information about DWL performance can be found in Pearson et al. (2009).

Simulated DWL wind profile observations were generated by adding an uncorrelated Gaussian random error ($1\sigma$ value of 0.3 m $s^{-1}$) to the wind magnitude at each level in the truth profile at a given profiler location. In clear-sky conditions, the profiles extend from the surface to the top of the BL whereas under cloudy conditions, the profiles are truncated at the cloud base if the cloud is located within the BL. The BL height was identified as the first location that the potential temperature increased by more than 1.5 K over a 100-m-deep layer in a given profile.

#### 3) RAM profiler observations

A research-grade RAM similar to the profiler currently deployed by the ARM Program at Lamont, Oklahoma, was chosen for this study. This system transmits pulses of 355-nm light into the atmosphere and then records the backscattered photons due to the vibrational-rotational Raman shift by water vapor and nitrogen molecules, with a maximum resolution of 7.5 m and 10 s (Goldsmith et al. 1998; Turner and Goldsmith 2005). The signal-to-noise ratio has a large diurnal cycle with greater noise occurring during the day as a result of the contamination by the background solar radiation. RAM profiles can extend through the entire troposphere at night but are generally limited to the lowest several kilometers during the day (Ferrare et al. 2006).

Prior studies (e.g., Turner and Goldsmith 1999; Ferrare et al. 2004) have shown that the water vapor mixing ratio is proportional to the ratio of the water vapor to nitrogen signals. The ambient temperature can also be inferred using measurements of the pure rotational Raman scattering by nitrogen and oxygen molecules since the shape of the rotational Raman spectrum changes with temperature. Two channels with slightly different spectral bandpasses can be used to measure this shape and thus determine the temperature. Following Di Girolamo et al. (2004), the ARM RAM profiles temperature by taking the ratio of the measured signal in the channels at 353 and 354 nm.

Simulated RAM temperature and water vapor profiles were calculated at each location by adding uncorrelated Gaussian random errors to the truth profiles that are a function of height and time of day (refer to Fig. 2 for $1\sigma$ error values). The simulated clear-sky nocturnal profiles extended to the tropopause (defined as 300 hPa) while the daytime profiles were truncated at 4-km AGL. Since the RAM laser beam is highly attenuated by clouds, the simulated profiles were terminated at the cloud base when clouds were present in the truth simulation.

#### 4) AERI observations

The AERI is a fully automated, commercially available passive spectrometer that measures downwelling atmospheric infrared radiation in the 3.3–19-$\mu$m range with very high spectral (1 $cm^{-1}$) and temporal (<30 s) resolution and better than 1% absolute radiometric accuracy (Knuteson et al. 2004a,b). The high-spectral resolution of the AERI provides sensitivity to the vertical distribution of moisture and temperature, which allows it to resolve up to 10 independent levels in the lower troposphere (Löhnert et al. 2009). The vertical resolution is much higher near the surface, with the number of independent levels decreasing with increasing water vapor content (e.g., Feltz et al. 1998, 2003).

Simulated AERI temperature and water vapor mixing ratio profiles were calculated at each location with the number of independent levels determined by the precipitable water vapor content. Random error profiles containing a correlated component were then added to the simulated AERI retrievals (refer to Fig. 2 for $1\sigma$ error values). For cloudy regions, the simulated profiles were calculated from the surface to 500 m below the cloud base while in clear-sky conditions the retrievals extended to 4 km AGL. Bias and root-mean-square difference profiles were computed for the simulated retrievals minus the truth profiles for both moist and dry conditions to ensure that the statistical profiles agreed with the analysis of Löhnert et al. (2009).

#### 5) MWR observations

An MWR is designed to measure the downwelling microwave radiation in several channels along the side

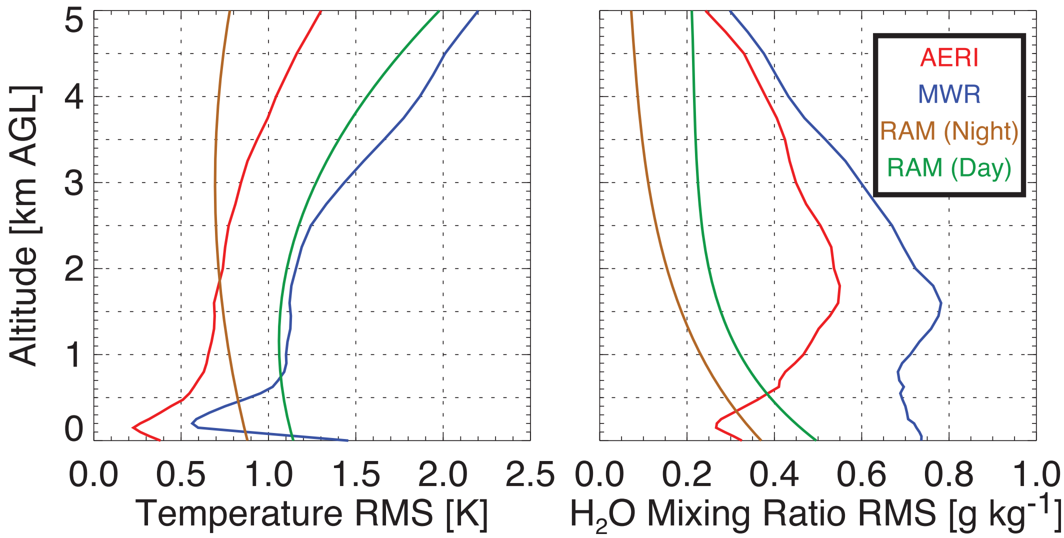


FIG. 2. The 1$\sigma$ measurement error profiles applied to the simulated (a) temperature (K) and (b) water vapor mixing ratio (g kg$^{-1}$) observations for the AERI (red), MWR (blue), and RAM (brown and green) sensors.

of a water vapor absorption line and several channels along the side of an oxygen absorption feature. Most commercially available MWR systems contain 5–7 channels near the 22.2-GHz water vapor absorption line and 5–7 channels near the 60-GHz oxygen absorption band. Measurements along these absorption features provide information about the thermodynamic structure of the atmosphere, with more opaque channels (i.e., where the atmosphere has a larger optical depth) sensitive to near-surface conditions while more transparent channels are sensitive to conditions farther away from the radiometer. Ground-based MWRs have been used for many years to retrieve profiles of temperature and humidity (e.g., Solheim et al. 1999). A detailed analysis by Löhnert et al. (2009) indicates that in clear-sky conditions the MWR provides 2 or 3 independent pieces of information in the humidity profile and 2–4 pieces in the temperature profile. An important advantage of the microwave profiling technique is that it is able to retrieve profiles in all sky conditions (i.e., the method is able to retrieve temperature and humidity profiles in clear and cloudy scenes) except for when liquid precipitation is present. The MWR profiles can also be used to provide an accurate "first guess" to improve higher-resolution AERI profile retrievals.

Simulated MWR temperature and humidity profiles were computed in a similar manner to the AERI profiles with both correlated and uncorrelated error components, including accounting for the change in the number of independent levels due to the total water vapor content. Unlike the AERI retrievals, however, the simulated MWR retrievals extend to 4 km AGL since nonprecipitating clouds do not interfere with the MWR signal. Figure 2 shows the 1$\sigma$ errors that were added to each profile.

6) OBSERVATION ERRORS

Observation errors used during the assimilation experiments include instrument and representativeness error components. For the conventional observations, the errors were based on those found in the operational dataset from the National Centers for Environmental Prediction. For the ASOS observations, the error was set to 2 K for temperature, 18% for relative humidity, and 2.5 m s$^{-1}$ for the horizontal wind. Errors of 1.8 K and 3.8 m s$^{-1}$ were used for the ACARS temperature and wind observations. The radiosonde errors varied with height and ranged from 0.8–1.2 K for temperature, 1.4–3.2 m s$^{-1}$ for the horizontal wind, and 10%–15% for relative humidity. For the profiler observations, the observation error was set to 0.45 m s$^{-1}$ for the DWL winds and to twice the 1$\sigma$ error value at a given level for the other observation types (refer to Fig. 2 for the error profiles).

## 3. Truth simulation

A high-resolution truth simulation tracking the evolution of several extratropical weather systems across the contiguous United States was performed using the WRF model. The simulation was initialized at 1200 UTC 6 January 2008 using 20-km Rapid Update Cycle (RUC) model analyses and then integrated for 48 h on a single 798 × 516 grid point domain (Fig. 1) containing 6-km horizontal resolution and 52 vertical levels. The vertical resolution decreased from <100 m in the lowest km to ~500 m at the model top, which was set to 65 hPa. Subgrid-scale processes were parameterized using the Thompson et al. (2008) mixed-phase cloud microphysics scheme, the Yonsei University (Hong et al. 2006) planetary boundary layer scheme, and the Dudhia (1989) shortwave and Rapid Radiative Transfer Model longwave (Mlawer et al. 1997) radiation schemes. Surface heat and moisture fluxes were calculated using the Noah land surface model. No cumulus parameterization scheme was used; therefore, all clouds were explicitly predicted by the microphysics scheme.

The evolution of the simulated surface and 500-hPa atmospheric conditions during the truth simulation is shown in Fig. 3. At 0000 UTC 7 January, a broad upper-level trough was located across the western United States (Fig. 3a) with a seasonably strong jet streak (50 m $s^{-1}$) extending across the central United States. A sharp southwest–northeast-oriented temperature gradient associated with a quasi-stationary surface boundary was also draped across this region. Strong southerly winds ahead of the surface front were transporting a plume of very moist air northward from the Gulf Coast into the Great Lakes region (Fig. 3b). By 1200 UTC, the 500-hPa trough had deepened slightly as it slowly propagated eastward and encountered a dominant ridge over the eastern United States (Fig. 3c). Strong southwesterly winds were still present across the central United States with a secondary jet maximum located along the western edge of the trough. The surface temperature gradient had weakened slightly across Kansas and Oklahoma while simultaneously extending farther to the northeast as the front strengthened over Michigan. The northward flow of warm moist air continued during this time period with the northern extent of the moist air confined to a slightly narrower corridor (Fig. 3d). Finally, by 0000 UTC 8 January, the trough had moved over the central Rocky Mountains while the downstream ridge remained stationary across the eastern United States (Fig. 3e). Two weak shortwave troughs were embedded within the southwesterly flow over the central United States. Very warm and moist air continued to stream northward in advance of the trough with mixing ratios in excess of 8 g $kg^{-1}$ present over a large portion of the eastern United States with localized maxima >12 g $kg^{-1}$ extending south and eastward from the Ozarks into the central Gulf of Mexico and Florida (Fig. 3f).

## 4. Assimilation results

### *a. Initial ensemble and model configuration*

The assimilation experiments described later in this section begin at 0000 UTC 7 January 2008. Initial conditions valid at this time were created for a 40-member WRF model ensemble using the following procedure, which is identical to that employed by Otkin (2010). Figure 4 shows the procedure in graphical form. First, an initial ensemble valid at 1200 UTC 5 January was created using the approach outlined by Torn et al. (2006). With this approach, balanced initial and lateral boundary perturbations were added to 40-km North American Mesoscale (NAM) model analyses for each ensemble member using covariance information provided by the WRF variational data assimilation system (WRF-Var). This ensemble was then integrated for 24 h to increase the ensemble spread. At that point, simulated ASOS and ACARS observations from the truth simulation were assimilated hourly until 0000 UTC 7 January, with simulated radiosonde observations also included at 0000 and 1200 UTC. This last step is used to produce an initial ensemble for the assimilation experiments containing flow-dependent covariance structures more representative of the atmospheric conditions in the truth simulation.

Assimilation experiments were performed for the same geographic domain as the truth simulation, but contained 18-km horizontal resolution and 37 vertical levels in order to better represent an operational setting. Unlike the truth simulation, the Kain and Fritsch (1990, 1993) subgrid-scale cumulus parameterization scheme was employed during the assimilation experiments. Different initialization datasets, grid resolutions, and parameterization schemes were chosen for the assimilation experiments to limit the risk of performing ‘‘identical twin’’ experiments.

In the remainder of this section, results from seven assimilation experiments and a control case without assimilation will be compared to data from the truth simulation. The experiments are designed to evaluate the relative impact of different ground-based profiler observations on the analysis accuracy. Table 1 shows the observation types assimilated during each experiment. Simulated conventional observations were the sole observations assimilated during the CONV case, but were also included in the other cases. DWL wind observations were assimilated during the CONV-DWL case, RAM temperature and water vapor mixing ratio observations during the CONV-RAM case, and then both DWL and RAM observations during the CONV-RD case. The DWL wind observations were then assimilated with temperature and moisture retrievals from the MWR and AERI during the CONV-MD and CONV-AD cases, respectively. Last, all of the AERI, MWR, and DWL observations were assimilated during the CONV-MAD case. Simulated radiosonde observations were assimilated at 0000 and 1200 UTC, whereas all other observation types were assimilated once per hour from 0000 UTC 7 January until 0000 UTC 8 January. Prognostic fields contained in the model state vector include the temperature, water vapor mixing ratio, horizontal

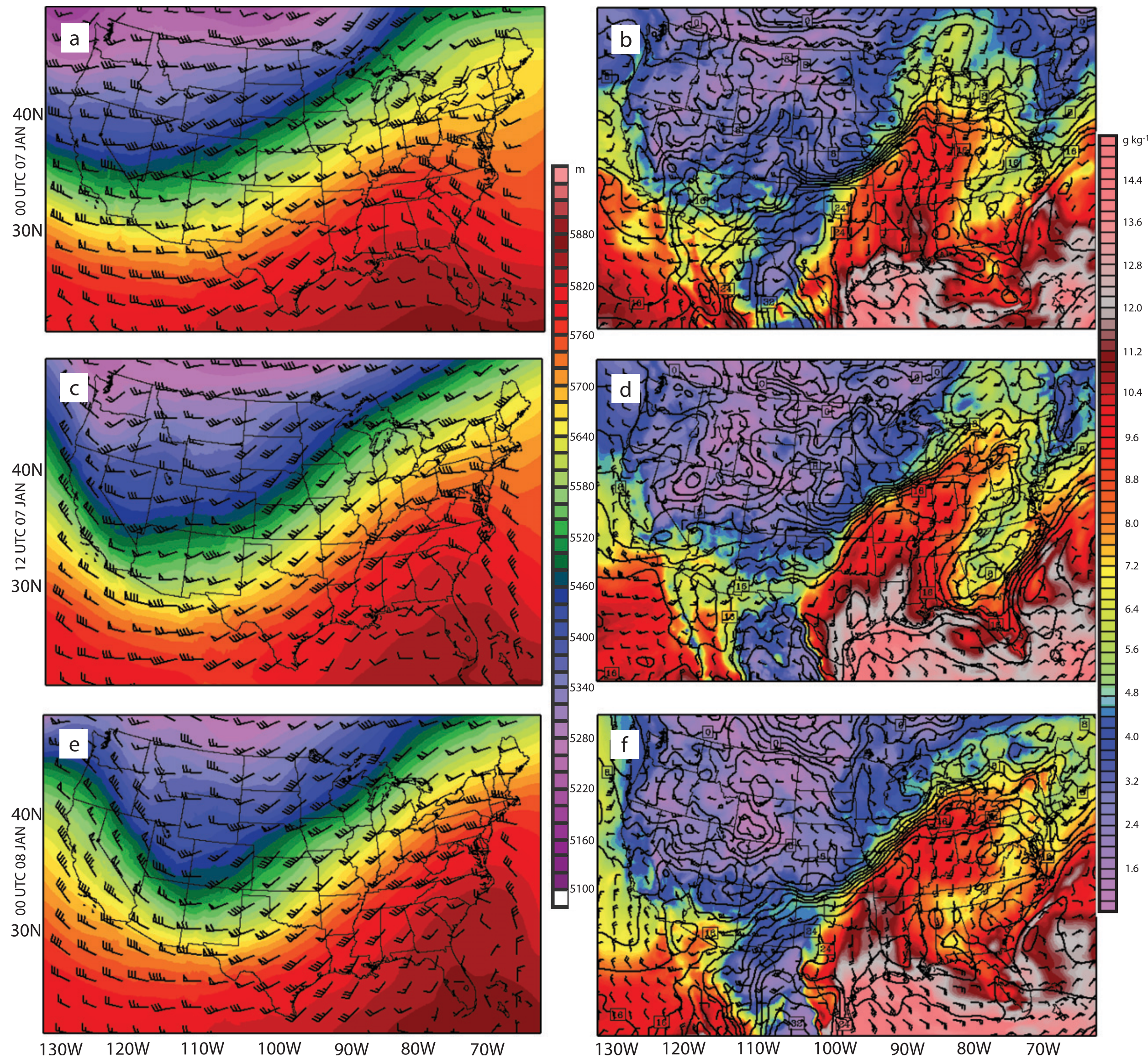


FIG. 3. (a) Simulated 500-hPa geopotential height (shaded every 20 m) and winds (m $s^{-1}$) valid at 0000 UTC 7 Jan 2008. (b) Simulated 100-m AGL water vapor mixing ratio (g $kg^{-1}$; shaded), winds (m $s^{-1}$), and temperature (K; contoured in black every 2°C) valid at 0000 UTC 7 Jan 2008. (c),(d) As in (a),(b), but for 1200 UTC 7 Jan 2008. (e),(f) As in (a),(b), but for 0000 UTC 8 Jan 2008.

and vertical wind components, surface pressure, number concentration of ice, and the mixing ratios for cloud water, rainwater, ice, snow, and graupel. The vertical and horizontal covariance localization half-radii were set to 3 and 200 km, respectively. The time and spatially varying inflation scheme developed by Anderson et al. (2009) was also used with the initial inflation factor set to 2%.

### *b. 850-hPa difference fields*

As a first step in evaluating the impact of the various observation types on the analysis accuracy, difference fields between the truth simulation and the posterior ensemble mean from each assimilation experiment were investigated. Output from the truth simulation was coarsened to 18-km resolution before the comparison. Figure 5 shows the 850-hPa temperature differences valid at the end of the assimilation period at 0000 UTC 8 January 2008. Inspection of the control case (Fig. 5a) shows that without data assimilation, a substantial cold temperature bias develops across most of the central United States due to a combination of stronger cold-air advection across the northern plains (not shown) and an eastward displacement of the surface boundary over Texas. Several

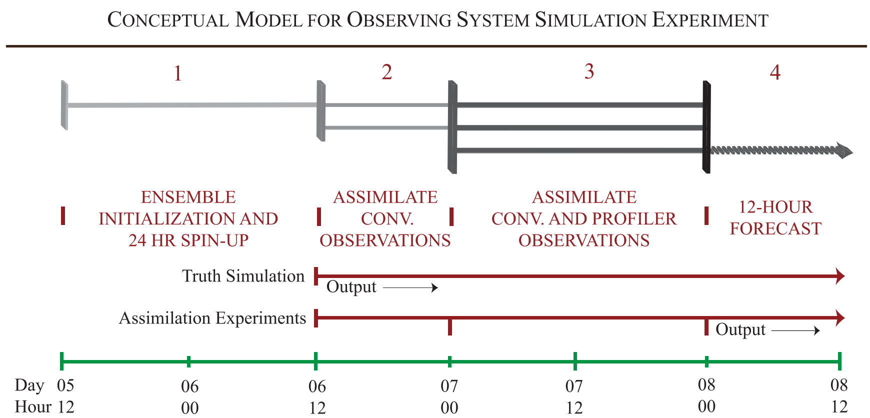


FIG. 4. Conceptual model for the OSSE. The first step is to generate an initial ensemble and then integrate it forward for 24 h. Conventional observations are assimilated during step 2 with both conventional and ground-based profiler observations assimilated during step 3. Finally, 12-h forecasts are performed during step 4.

smaller regions characterized by a warm temperature bias are also present across the eastern third of the domain and along the Pacific Coast. Assimilation of conventional observations reduces the cold temperature bias from Kansas to Minnesota, with smaller improvements occurring elsewhere (Fig. 5b). The temperature errors were further reduced, particularly across the central United States, when RAM observations were assimilated (Fig. 5c). The inclusion of wind data from the DWL had little or no impact on the temperature field (Fig. 5d); however, assimilation of the wind observations and the MWR or AERI profiles (Figs. 5e,f) reduced the temperature errors more than the CONV case but less than the CONV-RAM case. This behavior indicates that in the absence of explicit temperature observations from the RAM, MWR, or AERI, the covariance information associated with the DWL wind observations is unable to markedly improve the temperature analysis. When observations from multiple sensors are assimilated simultaneously (e.g., CONV-RD and CONV-MAD), however, the combination of high-quality wind and temperature observations produces a more accurate temperature analysis (Figs. 5g,h).

Figure 6 shows the 850-hPa vector wind errors for each case valid at 0000 UTC 8 January. Overall, the control case is characterized by much stronger winds than the truth simulation across most of the eastern half of the domain (Fig. 6a), with localized error maxima stretching from the upper Midwest into southern Canada and to the east of the lower Mississippi River Valley. The narrow band of weaker winds extending from eastern Texas northward to Missouri along with the band of stronger winds to the east indicate that the most intense southerly winds are located too far to the east due to an eastward displacement of the surface boundary. The vector wind errors were reduced in both regions during the CONV case (Fig. 6b); however, a band of weaker winds had developed near the surface boundary over Missouri. Minor improvements were made during the CONV-RAM case (Fig. 6c) with much better results achieved when DWL observations were assimilated (Fig. 6d). For instance, the eastward displacement of the strongest southerly winds over the south-central United States is no longer evident in the CONV-DWL case or in the other cases that included DWL assimilation. Combining the wind data with temperature and moisture

TABLE 1. Simulated observations assimilated during each experiment.

| Expt name | Assimilated observation types and variables |
|---|---|
| Control | No assimilation |
| CONV | Conventional observations (ASOS, radiosonde, ACARS) |
| CONV-DWL | DWL ($U$, $V$) + conventional observations |
| CONV-RAM | RAM ($T$, $Q$) + conventional observations |
| CONV-RD | RAM ($T$, $Q$) + DWL ($U$, $V$) + conventional observations |
| CONV-MD | MWR ($T$, $Q$) + DWL ($U$, $V$) + conventional observations |
| CONV-AD | AERI ($T$, $Q$) + DWL ($U$, $V$) + conventional observations |
| CONV-MAD | MWR ($T$, $Q$) + AERI ($T$, $Q$) + DWL ($U$, $V$) + conventional observations |

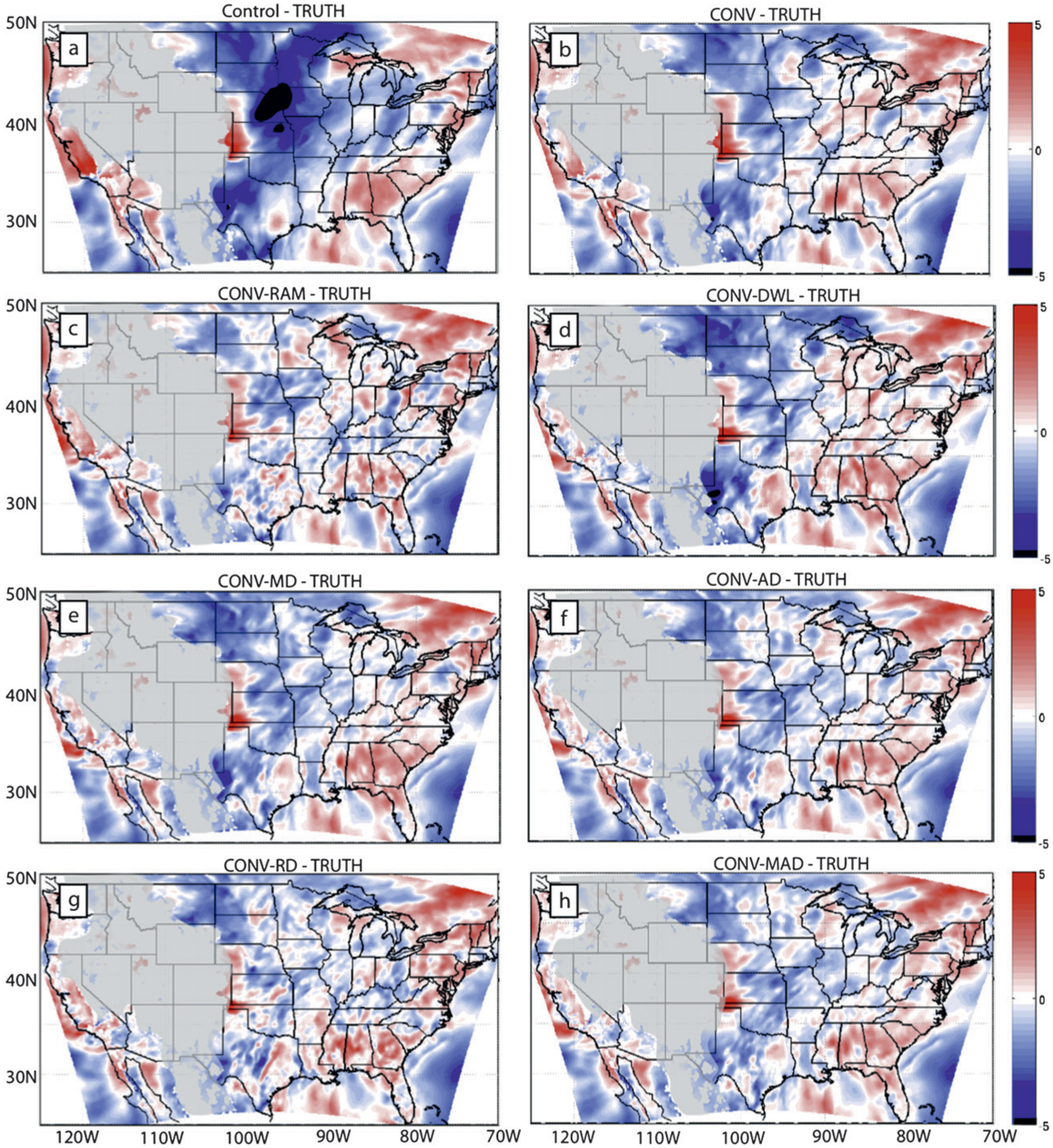


FIG. 5. 850-hPa temperature differences (K) computed by subtracting the truth from the (a) control, (b) CONV, (c) CONV-RAM, (d) CONV-DWL, (e) CONV-MD, (f) CONV-AD, (g) CONV-RD, and (h) CONV-MAD posterior ensemble mean valid at 0000 UTC 8 Jan 2008.

observations from the other sensors had only a minimal impact on the wind analyses (Figs. 6e–h).

Differences in the 850-hPa water vapor mixing ratio at 0000 UTC 8 January 2008 are shown in Fig. 7. In the control case (Fig. 7a), the eastward displacement of the surface boundary and strongest southerly winds over the south-central United States resulted in an eastward shift of the moisture advection from the Gulf of Mexico, which lead to the development of an extensive band of drier air from Texas to Iowa and too much moisture farther east. The error maxima were smaller over these regions during the CONV case (Fig. 7b), but the large

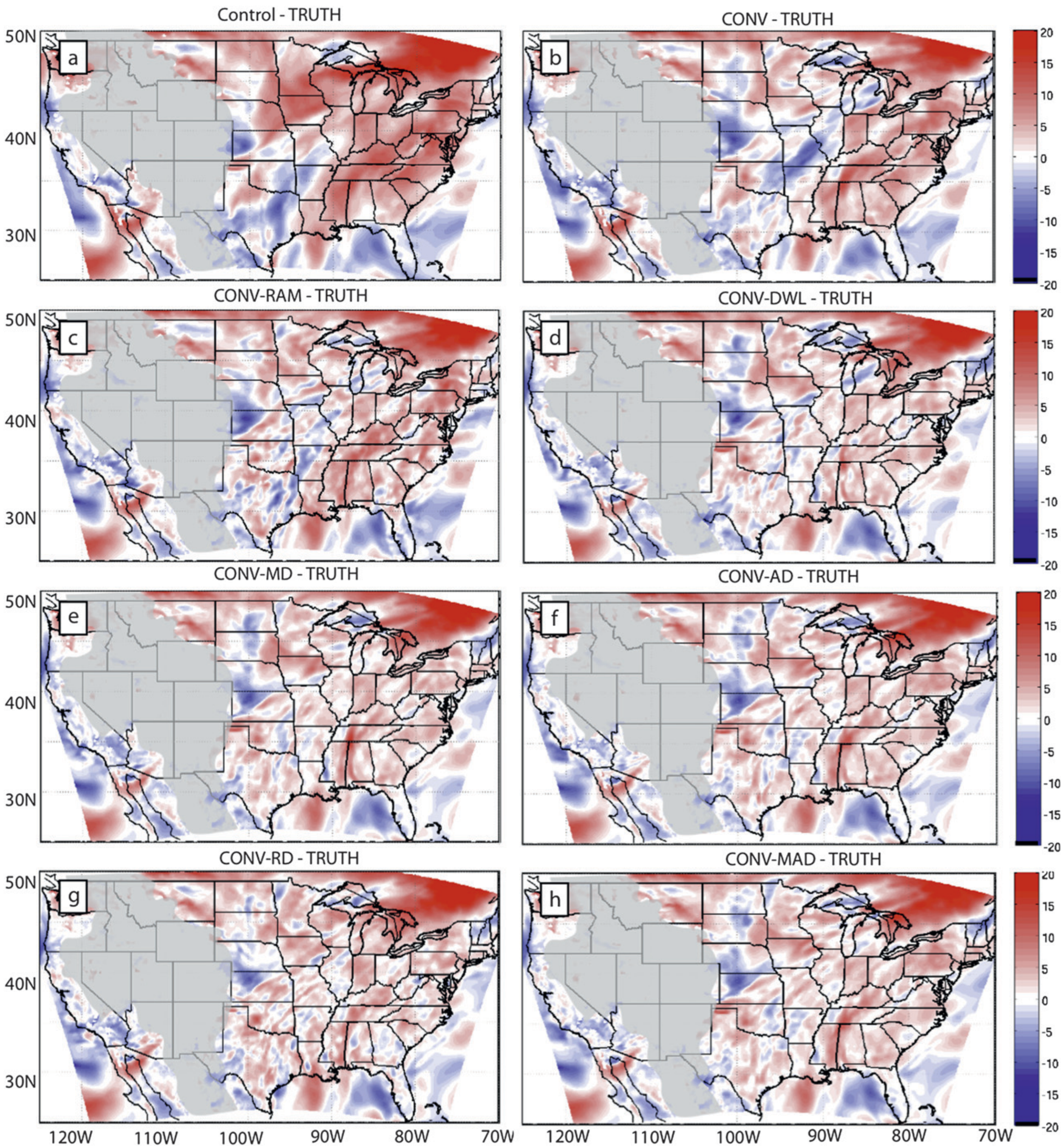


FIG. 6. 850-hPa vector wind differences (m $s^{-1}$) computed by subtracting the truth from the (a) control, (b) CONV, (c) CONV-RAM, (d), CONV-DWL, (e) CONV-MD, (f) CONV-AD, (g) CONV-RD, and (h) CONV-MAD posterior ensemble mean valid at 0000 UTC 8 Jan 2008.

dry bias over Georgia and South Carolina also expanded farther to the west relative to the control case. Moisture profiles from the RAM exerted a substantial positive impact on the analysis, with the overall extent of the errors reduced across the southern United States (Fig. 7c). Although assimilation of the DWL profiles greatly improved the wind analysis, these observations when used alone tended to degrade the moisture analysis in many areas with small improvements limited primarily to portions of the central United States (Fig. 7d). Noisy correlations between the wind observations and moisture field likely contributed to the larger errors; however,

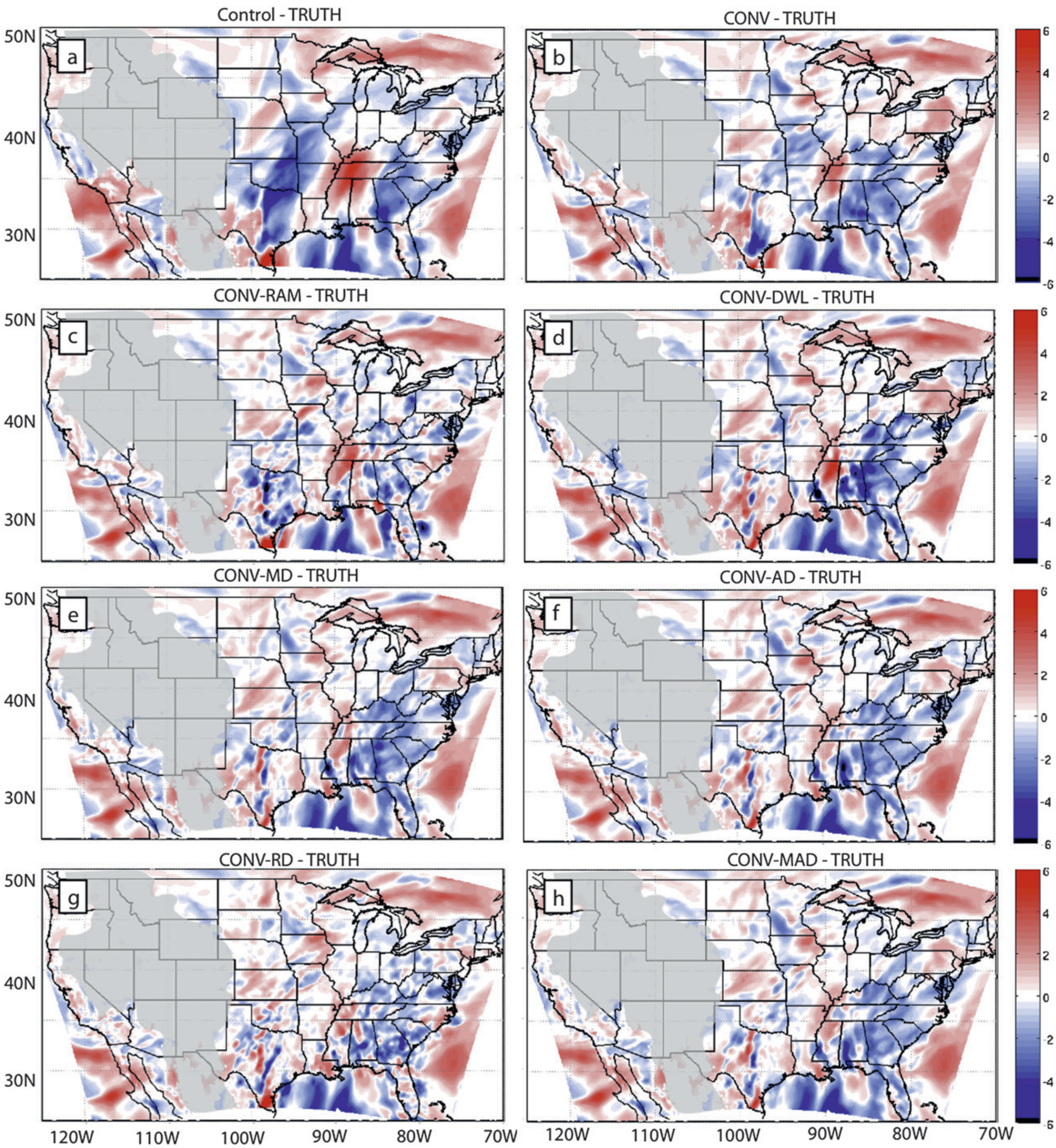


FIG. 7. 850-hPa water vapor mixing ratio differences (g $kg^{-1}$) computed by subtracting the truth from the (a) control, (b) CONV, (c) CONV-RAM, (d) CONV-DWL, (e) CONV-MD, (f) CONV-AD, (g) CONV-RD, and (h) CONV-MAD posterior ensemble mean valid at 0000 UTC 8 Jan 2008.

when both wind and moisture profiles were assimilated during the CONV-RD and CONV-MAD cases (Figs. 7g,h), the errors were generally less than when these observation types were assimilated separately. This positive synergy illustrates that a more accurate moisture analysis is dependent not only on the availability of accurate moisture observations but also on a better wind analysis and associated improvements in moisture advection. The presence of small-scale errors with larger amplitudes in the CONV-RD case may be due to the use of smaller observation errors for the RAM than for the MWR and AERI profiles (refer to Fig. 2), which will result in larger analysis increments that are generally beneficial but can also lead to localized areas containing larger errors. Using a different covariance localization radius for each observation type may help remedy this situation.

### *c. Probability distributions*

To examine the cumulative impact of the observations on the analysis by the middle and end of the assimilation period, error distributions were computed using differences between the truth simulation and the posterior ensemble mean for each assimilation experiment. The truth data was coarsened to 18-km resolution prior to computing the statistics with the outermost 10 grid points excluded from the analysis. Figure 8 shows the error distributions for 850-hPa temperature, water vapor mixing ratio and vector wind at 1200 UTC 7 January and 0000 UTC 8 January with standard statistical measures shown in Table 2. At 1200 UTC, the temperature distributions for the assimilation experiments exhibit a slightly higher peak shifted closer to the zero difference line (Fig. 8a), which indicates that the observations were able to remove some of the bias that had developed during the control case. Modest improvements made during the CONV case were enhanced through assimilation of MWR, AERI, and RAM temperature profiles but diminished somewhat when DWL observations were assimilated alone. The root-mean-square error (RMSE) and mean absolute error (MAE) were lowest during the CONV-RAM case (Table 2). By 0000 UTC (Fig. 8b), the control distribution had acquired a flatter shape with a higher percentage of grid points containing larger errors while the other cases maintained error distributions similar to those 12 h earlier. Though the bias was still lowest during the CONV-RAM case, the large separation between this case and the other experiments had decreased so that the overall statistics were similar between the CONV-RAM, CONV-AD, and CONV-MAD experiments. The smaller impact of the RAM observations by 0000 UTC may be due to their larger observation errors during the daytime (refer to Fig. 2), which diminishes their impact relative to the nighttime RAM observations and the other observation types. Inspection of the water vapor mixing ratio error distribution at 1200 UTC (Fig. 8c) shows that, with the exception of the CONV-RAM case, which contains a much higher percentage of small mixing ratio errors, relatively small differences exist between the assimilation cases. By 0000 UTC (Fig. 8d), all of the assimilation cases contain similar water vapor error distributions though the errors are slightly less for the CONV-AD and CONV-MAD cases (Table 2). Last, after 12 h of assimilation, small improvements were made to the vector wind error distribution during the CONV case, with further improvements realized when the profiler observations were also assimilated (Fig. 8e). The error statistics are slightly better when wind observations from the DWL are assimilated simultaneously with the MWR and AERI profiles; however, most of this improvement is due to the DWL observations (Table 2). By 0000 UTC, the vector wind errors had increased substantially during the control case with a peak near 7 m $s^{-1}$ (Fig. 8f). The CONV-RAM statistics were slightly worse than the CONV case, but assimilation of DWL observations during the other cases greatly improved the wind analysis with an error peak closer to 3 m $s^{-1}$ and a lower percentage of grid points containing large wind errors.

### *d. Mean error profiles*

Vertical profiles of bias and RMSE difference for temperature, relative humidity, and vector wind are shown in Fig. 9. The profiles were computed for each assimilation case using data from the posterior ensemble mean from each hourly assimilation cycle from 0000 UTC 7 January to 0000 UTC 8 January, and then subtracting the CONV error profiles from the profiles for the other cases. The truth data was coarsened to 18-km resolution prior to computing the statistics, with the outermost 10 grid points excluded from the analysis. Overall, the error statistics are generally better for the PBL profile assimilation experiments than for the CONV case, with the vertical extent and magnitude of the error reduction dependent upon which observations were assimilated. For temperature (Figs. 9a,b), the analysis accuracy was slightly degraded during the CONV-DWL case, most likely due to noisy correlations between the DWL wind observations and the unobserved temperature field. When AERI and MWR observations were also assimilated, the RMSE and bias were reduced in the lower troposphere, particularly during the CONV-AD and CONV-MAD cases, with the relative improvement diminishing with height and converging toward the CONV error profiles above 600 hPa. Comparison of the CONV-AD and CONV-MD profiles shows that the AERI observations were able to improve the temperature analysis more than the MWR observations; this is likely due to a combination of the higher information content in the AERI observations relative to the MWR observations and the higher occurrence of clear-sky AERI profiles during the assimilation period for this case. Last, assimilation of RAM observations during the CONV-RAM and CONV-RD cases resulted in the smallest errors overall, with especially large reductions in the upper troposphere relative to the other cases; however, this was not unexpected since the MWR and AERI observations were limited to heights below 4 km because of their lack of information content above that level.

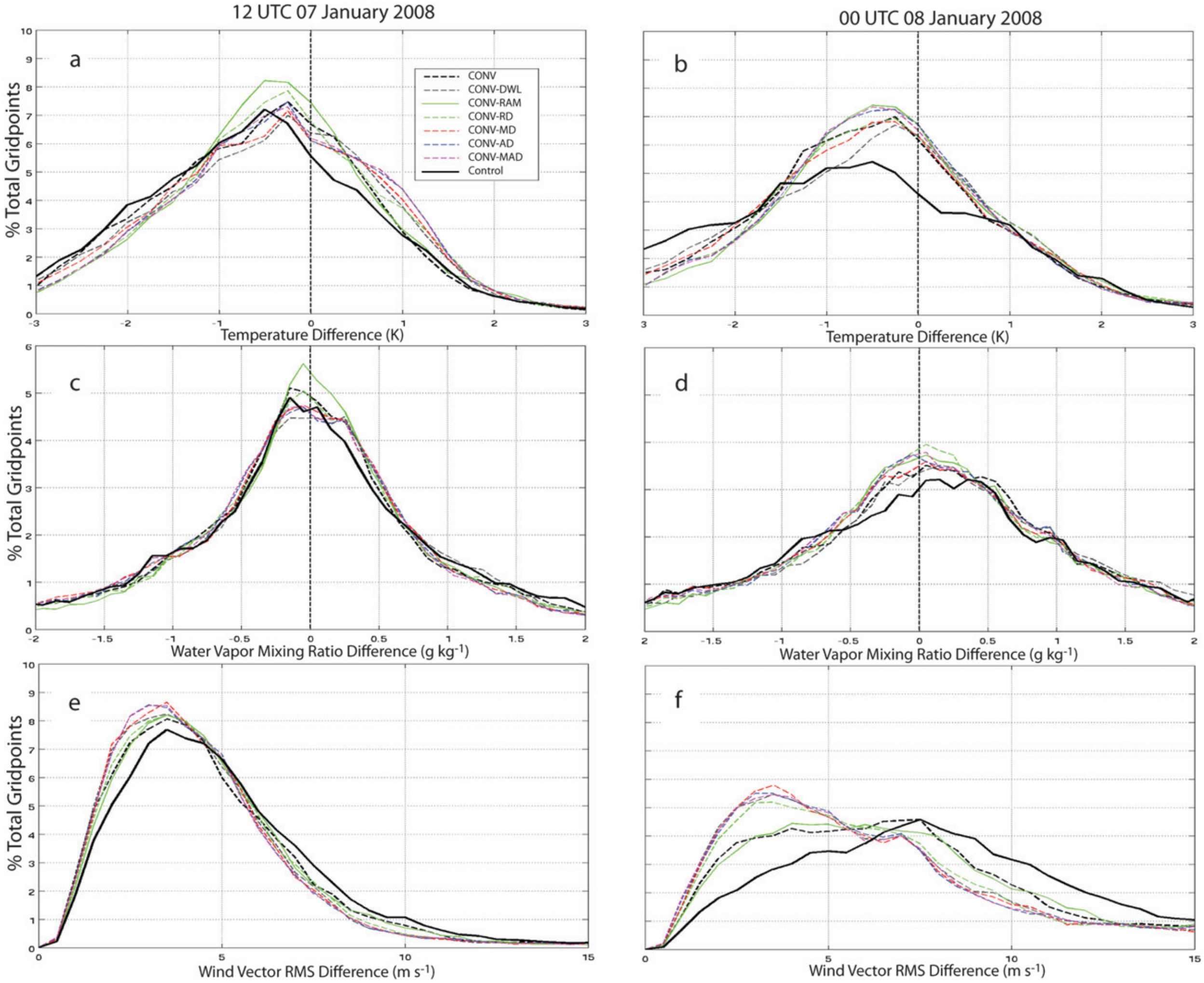


FIG. 8. (a) Probability density distributions computed for the difference between the 850-hPa temperature (K) from the posterior ensemble mean of each assimilation experiment and the truth simulation at 1200 UTC 7 Jan 2008. (b) As in (a), but valid at 0000 UTC 8 Jan 2008. (c) As in (a), but for 850-hPa mixing ratio differences (g $kg^{-1}$). (d) As in (c), but valid at 0000 UTC 8 Jan 2008. (e) As in (a), but for 850-hPa vector wind differences (m $s^{-1}$). (f) As in (e), but valid at 0000 UTC 8 Jan 2008.

Inspection of the relative humidity error profiles (Figs. 9c,d) shows that large error reductions occurred below 500 hPa when AERI profiles were assimilated, with only minimal changes occurring above this level. As was the case with the temperature field, the MWR observations alone had a smaller positive impact on the analysis than the AERI observations. Although the AERI is able to retrieve more independent pieces of information than the MWR, it is probable that the large separation between these two cases would decrease if more low-level clouds were present, thereby reducing the number of clear-sky AERI retrievals. RAM observations had by far the greatest impact on the moisture analysis with the largest error reductions occurring at almost all levels during the CONV-RAM and CONV-RD cases. The substantial impact of these observations in the upper troposphere is particularly noteworthy and sharply contrasts with the minimal ability of the other observation types to improve the upper-level moisture analysis. DWL wind observations tended to degrade the analysis during the CONV-DWL case, which indicates that more accurate covariances between the small-scale wind and moisture fields are necessary to reduce errors in the moisture field. The negative synergy between the wind observations and the moisture field would likely be reduced for a larger ensemble size that is better able to capture small-scale correlations between these variables.

For the vector wind field (Fig. 9e), minor differences exist between the CONV-DWL case and the other assimilation cases below 400 hPa (with the exception of

TABLE 2. RMSE, MAE, and bias computed for 850-hPa temperature (K), water vapor mixing ratio (g kg$^{-1}$), and vector wind (m s$^{-1}$) at 1200 UTC 7 Jan 2008 and 0000 UTC 8 Jan 2008. The statistics were computed using data from the posterior ensemble mean of each assimilation experiment. Boldface numbers indicate cases with the smallest errors for each variable.

| | RMSE | MAE | Bias | RMSE | MAE | Bias |
|---|---|---|---|---|---|---|
| Expt | 1200 UTC 7 Jan 2008 | | | 0000 UTC 8 Jan 2008 | | |
| | | | 850-hPa temperature (K) | | | |
| Control | 1.610 | 1.211 | −0.623 | 1.912 | 1.504 | −0.758 |
| CONV | 1.400 | 1.056 | −0.485 | 1.368 | 1.070 | −0.359 |
| CONV-DWL | 1.438 | 1.090 | −0.356 | 1.477 | 1.147 | −0.388 |
| CONV-RAM | **1.236** | **0.917** | −0.291 | **1.283** | **0.992** | **−0.223** |
| CONV-RD | 1.281 | 0.970 | −0.268 | 1.306 | 1.023 | −0.249 |
| CONV-MD | 1.380 | 1.057 | −0.311 | 1.384 | 1.083 | −0.358 |
| CONV-AD | 1.314 | 1.005 | −0.241 | **1.279** | **0.989** | −0.283 |
| CONV-MAD | 1.308 | 1.000 | **−0.233** | **1.283** | **0.994** | −0.279 |
| | | | 850-hPa water vapor mixing ratio (g kg$^{-1}$) | | | |
| Control | 1.072 | 0.786 | 0.016 | 1.500 | 1.108 | 0.099 |
| CONV | **0.989** | 0.724 | 0.001 | 1.301 | 0.967 | 0.168 |
| CONV-DWL | 1.053 | 0.771 | 0.061 | 1.412 | 1.034 | 0.211 |
| CONV-RAM | 1.011 | **0.711** | 0.039 | 1.345 | 0.958 | 0.187 |
| CONV-RD | 1.020 | 0.740 | 0.037 | 1.324 | 0.943 | 0.186 |
| CONV-MD | 1.004 | 0.732 | **0.000** | 1.311 | 0.966 | 0.130 |
| CONV-AD | 0.995 | 0.731 | −0.007 | **1.275** | **0.929** | 0.134 |
| CONV-MAD | 0.996 | 0.731 | −0.019 | **1.275** | **0.930** | **0.116** |
| | | | 850-hPa vector wind (m s$^{-1}$) | | | |
| | Vector RMSE | Magnitude MAE | Vector Bias | Vector RMSE | Magnitude MAE | Vector Bias |
| Control | 5.33 | 2.73 | 0.95 | 8.74 | 4.85 | 5.90 |
| CONV | 4.74 | 2.71 | **0.23** | 6.45 | 3.30 | 3.51 |
| CONV-DWL | **4.22** | **2.19** | 0.91 | 5.57 | **2.81** | **2.68** |
| CONV-RAM | 4.78 | 2.60 | 0.53 | 6.61 | 3.33 | 3.53 |
| CONV-RD | 4.43 | 2.35 | 1.01 | 5.75 | 2.96 | 2.89 |
| CONV-MD | **4.20** | **2.20** | 1.00 | **5.49** | **2.83** | 2.85 |
| CONV-AD | **4.24** | **2.17** | 1.04 | 5.57 | 2.89 | 2.97 |
| CONV-MAD | **4.25** | **2.17** | 1.08 | 5.54 | 2.89 | 3.00 |

CONV-RAM), which indicates that much of the improved performance relative to the CONV case is due to the DWL wind observations. Although the RAM temperature and moisture observations did not improve the wind analysis below 600 hPa during the CONV-RAM case, the errors do start to diminish above this level and become smaller than the other cases above 400 hPa. The varying impact of the RAM observations with height is likely due to the cumulative effect of the larger improvements made to the temperature analysis during this case and their indirect affect on the wind field through mass balance constraints.

## 5. Discussion and conclusions

In this study, a regional-scale OSSE was used to examine how the assimilation of temperature, water vapor, and horizontal wind profiles from an array of surface-based remote sensing boundary layer profiling sensors impacts the accuracy of regional atmospheric analyses at mesoscale resolution. Assimilation experiments were conducted using the EnKF algorithm implemented in the DART data assimilation system. The case study tracked the evolution of several extratropical weather systems that occurred across the contiguous United States during 7–8 January 2008. A high-resolution ''truth'' simulation containing realistic cloud and thermodynamic properties was performed using the WRF model. Data from this simulation was used to generate simulated vertical profiles of temperature, water vapor, and winds emulating observations from a potential array of DWL, RAM, MWR, and AERI sensors located at existing WSR-88D radar locations. Simulated conventional radiosonde, surface, and aircraft pilot observations were also generated. Realistic errors based on a given sensor's accuracy specifications, including vertically correlated errors when appropriate, were added to each observation. Seven assimilation experiments were conducted with various combinations of observations assimilated once per hour during a 24-h period.

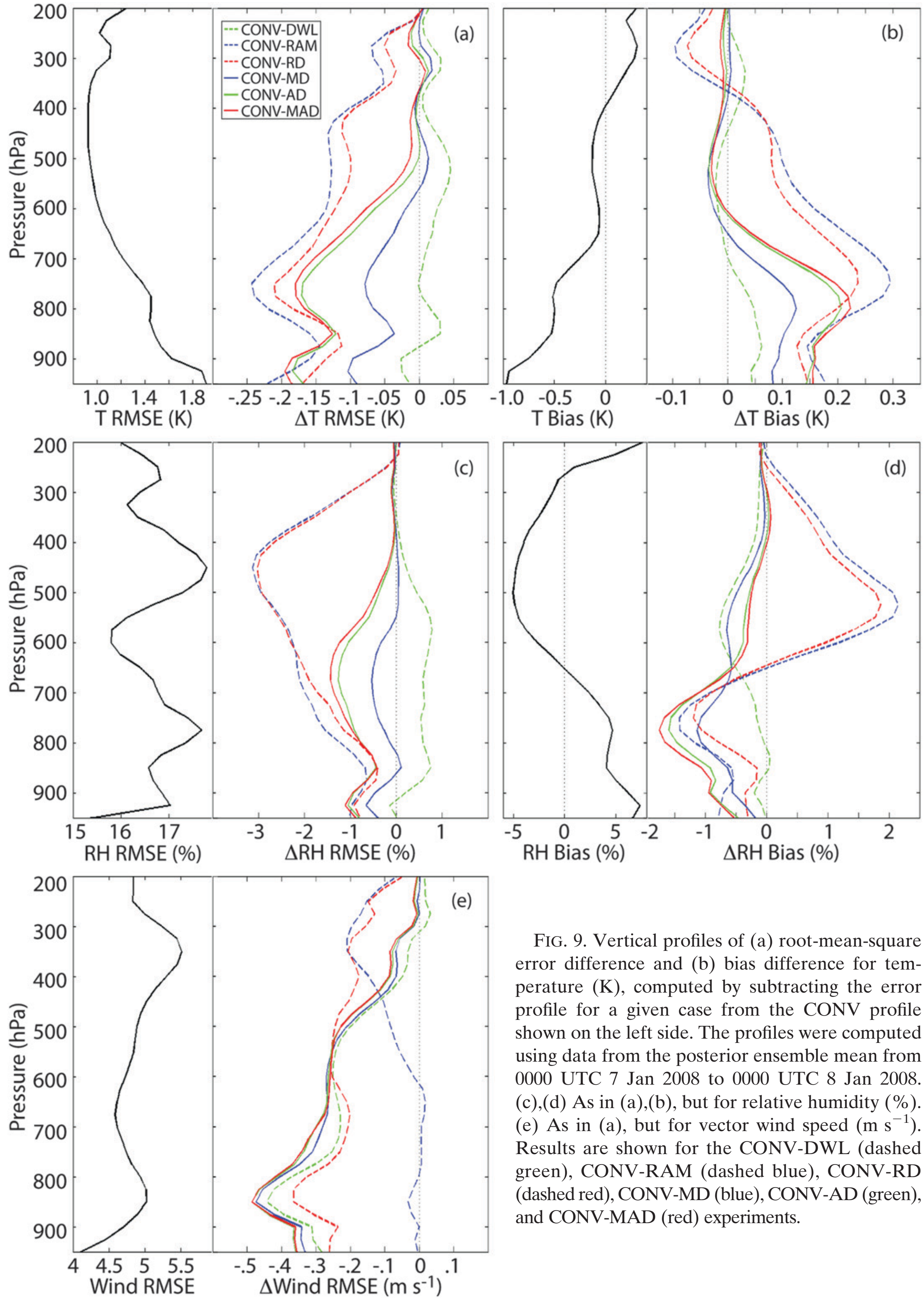


FIG. 9. Vertical profiles of (a) root-mean-square error difference and (b) bias difference for temperature (K), computed by subtracting the error profile for a given case from the CONV profile shown on the left side. The profiles were computed using data from the posterior ensemble mean from 0000 UTC 7 Jan 2008 to 0000 UTC 8 Jan 2008. (c),(d) As in (a),(b), but for relative humidity (%). (e) As in (a), but for vector wind speed (m $s^{-1}$). Results are shown for the CONV-DWL (dashed green), CONV-RAM (dashed blue), CONV-RD (dashed red), CONV-MD (blue), CONV-AD (green), and CONV-MAD (red) experiments.

Overall, the results demonstrate that the assimilation of high-quality observations from an array of surface-based profiling systems within an advanced data assimilation system has the potential to improve the accuracy of atmospheric analyses used by numerical weather prediction models and operational forecasters. The impact of each profiling system was greatest on the variables either observed or retrieved by that instrument in the lower and middle troposphere, though some minor improvements also occurred in the unobserved variables and in the upper troposphere, particularly when RAM observations were assimilated. Comparison of the 850-hPa difference fields between the truth simulation and each assimilation experiment showed that the research-quality RAM temperature and moisture observations greatly improved the final temperature and humidity analyses, but had little or no impact on the wind field. AERI and MWR profiles also improved the temperature and moisture analyses in the lower troposphere, but had a slightly smaller impact than the RAM assimilation cases. DWL wind observations, however, tended to slightly degrade the accuracy of the temperature and moisture analyses, but had a large positive impact on the wind field. For instance, the eastward displacement of the strongest southerly winds ahead of the surface boundary was removed when DWL wind profiles were assimilated. Further improvements were made to the wind field when temperature and moisture observations from the other sensors were assimilated simultaneously with the wind data, which illustrates that the availability of accurate mass profiles in the lower troposphere is also important for improving mesoscale wind analyses. A similar beneficial synergy between sensors occurred in the moisture field where the best analysis was achieved during the CONV-RD and CONV-MAD cases. The tendency for the errors to be smallest when both moisture and wind observations are assimilated demonstrates that a more accurate moisture analysis is dependent not only on the availability of accurate moisture observations, but also on a better wind analysis and associated improvements in moisture advection between analysis times. Factor separation techniques (Stein and Alpert 1993; Rostkier-Edelstein and Hacker 2010) could be used to further quantify the synergism between the observed and unobserved variables in future studies.

Inspection of vertical profiles of bias and RMSE computed using data from the entire 24-h assimilation period showed that the vertical extent and magnitude of the error reduction for a given field is dependent upon which observations are assimilated. The smallest temperature and moisture errors generally occurred during the CONV-RAM and CONV-RD cases, particularly in the upper troposphere where the errors were much less than the other cases; however, this is not surprising given that the information content in the AERI and MWR observations is minimal above 600 hPa. Comparison of the CONV-AD and CONV-MD results shows that the AERI observations had a larger impact than the MWR observations on the temperature and moisture fields. Although the AERI provides more independent pieces of information, the large difference between these two sensors would possibly be reduced if more low-level clouds were present, thereby reducing the number of clear-sky AERI retrievals. DWL observations greatly improved the wind analyses in the lower and middle troposphere; however, the accuracy of the temperature and moisture fields tended to decrease, which indicates that more accurate covariances are necessary to reduce errors in the unobserved fields when these observations are assimilated. The assimilation of RAM observations did not improve the wind analysis below 600 hPa; however, the errors started to diminish above this level and actually became smaller than the other cases above 400 hPa. The greater impact of these observations in the upper troposphere is likely due to the cumulative effect of the larger improvements made to the temperature analysis and their indirect affect on the wind field through mass balance constraints.

In Part II of this study (Hartung et al. 2011), the impact of the various observation types will be further evaluated through a comparison of their impact on short-range (0–12 h) ensemble forecasts of accumulated precipitation and temperature, moisture, and winds in the lower troposphere (i.e., step 4 in Fig. 4). The forecast results indicate that the simultaneous assimilation of wind profiles from the DWL and moisture and temperature profiles from the RAM, AERI, or MWR produces the largest forecast improvements, which is consistent with the atmospheric analysis results presented in this study. Future work includes performing a similar study but with higher model resolution for a summertime convective case to evaluate the impact of the observations on convective initiation and thunderstorm evolution. Additional studies containing either half or double the profiler density will also be performed to help determine how many profiler locations are necessary from a cost–benefit perspective to optimally improve the analysis accuracy and forecast skill.

*Acknowledgments.* This work was funded by the National Oceanic and Atmospheric Administration in support of recommendation 8a in National Research Council (2009). The assimilation experiments leveraged computer resources purchased by GOES-R research projects at the Cooperative Institute for Meteorological Satellite Studies at the University of Wisconsin—Madison. Comments from two anonymous reviewers helped improve the manuscript.

## REFERENCES

Anderson, J. L., 2001: An ensemble adjustment Kalman filter for data assimilation. *Mon. Wea. Rev.,* **129,** 2884–2903.

——, 2007: An adaptive covariance inflation error correction algorithm for ensemble filters. *Tellus,* **59A,** 210–224.

——, 2009: Spatially and temporally varying adaptive covariance inflation for ensemble filters. *Tellus,* **61A,** 72–83.

——, T. Hoar, K. Raeder, H. Liu, N. Collins, R. Torn, and A. Avellano, 2009: The Data Assimilation Research Testbed: A community facility. *Bull. Amer. Meteor. Soc.,* **90,** 1283–1296.

Arnold, C. P., and C. H. Dey, 1986: Observing-systems simulation experiments: Past, present, and future. *Bull. Amer. Meteor. Soc.,* **67,** 687–695.

Benjamin, S. G., K. A. Brewster, R. Brümmer, B. F. Jewett, T. W. Schlatter, T. L. Smith, and P. A. Stamus, 1991: An isentropic 3-hourly data assimilation system using ACARS aircraft observations. *Mon. Wea. Rev.,* **119,** 888–906.

Di Girolamo, P., R. Marchese, D. N. Whiteman, and B. B. Demoz, 2004: Rotational Raman lidar measurements of atmospheric temperature in the UV. *Geophys. Res. Lett.,* **31,** L01106, doi:10.1029/2003GL018342.

Dudhia, J., 1989: Numerical study of convection observed during the winter monsoon experiment using a mesoscale two-dimensional model. *J. Atmos. Sci.,* **46,** 3077–3107.

Evensen, G., 1994: Sequential data assimilation with a nonlinear quasi-geostrophic model using Monte Carlo methods to forecast error statistics. *J. Geophys. Res.,* **99** (C5), 10 143–10 162.

Feltz, W. F., W. L. Smith, R. O. Knuteson, H. E. Revercomb, H. M. Woolf, and H. B. Howell, 1998: Meteorological applications of temperature and water vapor retrievals from the ground-based Atmospheric Emitted Radiance Interferometer (AERI). *J. Appl. Meteor.,* **37,** 857–875.

——, H. B. Howell, R. O. Knuteson, H. M. Woolf, and H. E. Revercomb, 2003: Near continuous profiling of temperature, moisture, and atmospheric stability using the Atmospheric Emitted Radiance Interferometer (AERI). *J. Appl. Meteor.,* **42,** 584–597.

Ferrare, R. A., and Coauthors, 2004: Characterization of upper-troposphere water vapor measurements during AFWEX using LASE. *J. Atmos. Oceanic Technol.,* **21,** 1790–1808.

——, and Coauthors, 2006: Evaluation of daytime measurements of aerosols and water vapor made by an operational Raman lidar over the Southern Great Plains. *J. Geophys. Res.,* **111,** D05S08, doi:10.1029/2005JD005836.

Gaspari, G., and S. E. Cohn, 1999: Construction of correlation functions in two and three dimensions. *Quart. J. Roy. Meteor. Soc.,* **125,** 723–757.

Goldsmith, J. E. M., F. H. Blair, S. E. Bisson, and D. D. Turner, 1998: Turn-key Raman lidar for profiling atmospheric water vapor, clouds, and aerosols. *Appl. Opt.,* **37,** 4979–4990.

Hamill, T. M., J. S. Whitaker, and C. Snyder, 2001: Distance-dependent filtering of background error covariance estimates in an ensemble Kalman filter. *Mon. Wea. Rev.,* **129,** 2776–2790.

Hartung, D. C., J. A. Otkin, R. A. Petersen, D. D. Turner, and W. F. Feltz, 2011: Assimilation of surface-based boundary layer profiler observations during a cool-season weather event using an Observing System Simulation Experiment. Part II: Forecast assessment. *Mon. Wea. Rev.,* **139,** 2327–2346.

Hong, S.-Y., Y. Noh, and J. Dudhia, 2006: A new vertical diffusion package with an explicit treatment of entrainment processes. *Mon. Wea. Rev.,* **134,** 2318–2341.

Kain, J. S., and J. M. Fritsch, 1990: A one-dimensional entraining detraining plume model and its application in convective parameterization. *J. Atmos. Sci.,* **47,** 2784–2802.

——, and ——, 1993: Convective parameterization for mesoscale models: The Kain-Fritsch scheme. *The Representation of Cumulus Convection in Numerical Models,* K. A. Emanuel and D. J. Raymond, Eds., Amer. Meteor. Soc., 165–170.

Knuteson, R. O., and Coauthors, 2004a: Atmospheric Emitted Radiance Interferometer. Part I: Instrument design. *J. Atmos. Oceanic Technol.,* **21,** 1763–1776.

——, and Coauthors, 2004b: Atmospheric Emitted Radiance Interferometer. Part II: Instrument performance. *J. Atmos. Oceanic Technol.,* **21,** 1777–1789.

Kuo, Y.-H., and Y.-R. Guo, 1989: Dynamic initialization using observations from a hypothetical network of profilers. *Mon. Wea. Rev.,* **117,** 1975–1998.

——, E. G. Donall, and M. A. Shapiro, 1987: Feasibility of short-range numerical weather prediction using observations from a network of wind profilers. *Mon. Wea. Rev.,* **115,** 2402–2427.

Löhnert, U., D. D. Turner, and S. Crewell, 2009: Ground-based temperature and humidity profiling using spectral infrared and microwave observations. Part I: Simulated retrieval performance in clear-sky conditions. *J. Appl. Meteor. Climatol.,* **48,** 1017–1032.

Mitchell, H. L., P. L. Houtekamer, and G. Pellerin, 2002: Ensemble size, balance, and model-error representation in an ensemble Kalman filter. *Mon. Wea. Rev.,* **130,** 2791–2808.

Mlawer, E. J., S. J. Taubman, P. D. Brown, and M. J. Iacono, 1997: Radiative transfer for inhomogeneous atmospheres: RRTM, a validated correlated-k model for the longwave. *J. Geophys. Res.,* **102,** 16 663–16 682.

Moninger, W. R., S. G. Benjamin, B. D. Jamison, T. W. Schlatter, T. L. Smith, and E. J. Szoke, 2010: Evaluation of regional aircraft observations using TAMDAR. *Wea. Forecasting,* **25,** 627–645.

National Research Council, 2009: *Observing Weather and Climate from the Ground Up: A Nationwide Network of Networks*. The National Academies Press, 250 pp. [Available online at http://www.nap.edu/catalog/12540.html.]

Otkin, J. A., 2010: Clear and cloudy sky infrared brightness temperature assimilation using an ensemble Kalman filter. *J. Geophys. Res.,* **115,** D19207, doi:10.1029/2009JD013759.

Pearson, G., F. Davies, and C. Collier, 2009: An analysis of the performance of the UFAM pulsed Doppler lidar for observing the boundary layer. *J. Atmos. Oceanic Technol.,* **26,** 240–250.

Rostkier-Edelstein, D., and J. P. Hacker, 2010: The roles of surface-observation ensemble assimilation and model complexity for nowcasting of PBL profiles: A factor separation analysis. *Wea. Forecasting,* **25,** 1670–1690.

Skamarock, W. C., J. B. Klemp, J. Dudhia, D. O. Gill, D. M. Barker, W. Wang, and J. G. Powers, 2005: A description of the Advanced Research WRF version 2. NCAR Tech. Note/TN-468+STR, 88 pp.

Solheim, F. S., J. Vivekanandan, R. H. Ware, and C. Rocken, 1999: Propagation delays induced in GPS signals by dry air, water vapor, hydrometeors, and other particulates. *J. Geophys. Res.,* **104,** 9663–9670.

Stein, U., and P. Alpert, 1993: Factor separation in numerical simulations. *J. Atmos. Sci.,* **50,** 2107–2115.

Thompson, G., P. R. Field, R. M. Rasmussen, and W. D. Hall, 2008: Explicit forecasts of winter precipitation using an improved bulk microphysics scheme. Part II: Implementation of a new snow parameterization. *Mon. Wea. Rev.,* **136,** 5095–5115.

Torn, R. D., G. J. Hakim, and C. Snyder, 2006: Boundary conditions for limited-area ensemble Kalman filters. *Mon. Wea. Rev.,* **134,** 2490–2502.

Turner, D. D., and J. E. M. Goldsmith, 1999: Twenty-four-hour Raman lidar water vapor measurements during the Atmospheric

Radiation Measurement Program's 1996 and 1997 water vapor intensive observation periods. *J. Atmos. Oceanic Technol.,* **16,** 1062–1076.

——, and ——, 2005: The refurbishment and upgrade of the Atmospheric Radiation Measurement Raman lidar. *Proc. 15th Atmospheric Radiation Measurement (ARM) Science Team Meeting*, Daytona Beach, FL, ARM, 6 pp. [Available online at http://www.arm.gov/publications/proceedings/conf15/extended_abs/turner_dd1.pdf.]

——, W. F. Feltz, and R. A. Ferrare, 2000: Continuous water vapor profiles from operational ground-based active and passive remote sensors. *Bull. Amer. Meteor. Soc.,* **81,** 1301–1317.

——, R. A. Ferrare, L. A. Heilman Brasseur, W. F. Feltz, and T. P. Tooman, 2002: Automated retrievals of water vapor and aerosol profiles from an operational Raman lidar. *J. Atmos. Oceanic Technol.,* **19,** 37–50.

Whitaker, J. S., and T. M. Hamill, 2002: Ensemble data assimilation without perturbed observations. *Mon. Wea. Rev.,* **130,** 1913–1924.